# Ultrafast three dimensional imaging of lattice dynamics in gold nanocrystals

J. N. Clark[1], L. Beitra[1], G. Xiong[1], A. Higginbotham[2], D. M. Fritz[3], H. T. Lemke[3], D. Zhu[3], M. Chollet[3], G. J. Williams[3], M. Messerschmidt[3], B. Abbey[4], R. J. Harder[5], A. M. Korsunsky[6,7], J. S. Wark[2] & I. K. Robinson[1,7]

[1]*London Centre for Nanotechnology, University College, London WC1E 6BT, UK*

[2]*Department of Physics, Clarendon Laboratory, University of Oxford, Parks Road, Oxford OX1 3PU, UK*

[3]*Linac Coherent Light Source, SLAC National Accelerator Laboratory, 2575 Sand Hill Road, Menlo Park, California 94025, USA*

[4]*ARC Centre of Excellence for Coherent X-ray Science, Department of Physics, La Trobe University, Bundoora, Victoria 3086, Australia*

[5]*Advanced Photon Source, Argonne, IL 60439, USA*

[6]*Department of Engineering Science, University of Oxford, Parks Road, Oxford OX1 3PJ, UK*

[7]*Research Complex at Harwell, Didcot, Oxfordshire OX11 0DE, UK*

**Key insights into the behaviour of materials can be gained by observing their structure during phase transitions or when they undergo lattice distortion. Laser pulses on the femtosecond time scale can be used to induce disorder in a "pump-probe" experiment with the subsequent transients being probed stroboscopically using femtosecond pulses of visible light [1], X-rays [2] or electrons [3]. Using these techniques, many fundamental phenomena have been**

observed, such as non-thermal melting in semiconductors [4], thermal melting in metals [5] and bond softening [6]. However, until now, it has been impossible to resolve these phenomena fully in three dimensions, on nanometre length scales and femotsecond time scales. Here we capitalise on recent developments in X-ray free electron sources [7], which extended the capabilities of ultra-fast X-ray diffraction by providing even brighter and shorter pulses with the added property that the X-rays are highly coherent. This has already allowed coherent diffraction imaging [8] of single particle structures [9] and weakly scattering biological samples [10]. Here we report three dimensional imaging of the generation and subsequent evolution of coherent acoustic phonons on the picosecond time scale within a single gold nanocrystal using an X-ray free electron laser, providing valuable insights into the fundamental physics of this phenomenon. In the broader context this work will find immediate applications in the imaging of phonons in semiconductors as well as samples undergoing phase transitions[11], providing access to structure with unprecedented temporal and spatial resolution.

Coherent lattice vibrations (phonons) in solids play an important role in many phenomena such as melting [2,5,12,13], phase transitions [11] as well as ferroelectric materials [14]. Ultrashort (femtosecond) laser pulses have been used to reveal great detail about the dynamics of these phenomena, however, many of these studies have been confined to bulk samples or ensembles of nanoparticles. With nanoparticles playing an increasingly important role in technology, from catalysis [15] and photonic devices [16] to single particle mass spectrometry [17] and sensing, understanding their mechanical and dynamical properties becomes very important as many of the processes occur over femtosecond (fs) and picosecond (ps) timescales.

Characterisation of lattice displacements in individual nanoparticles over very short time scales with atomic sensitivity has so far been elusive. The interrogation of individual particles is important, as sample heterogeneity can give the effect of significantly shorter-lived dynamics than actually exist [18,19] and may hide the presence of high order phonon modes or anharmonicity. Optical pump-probe experiments have shown promising results , particularly for single particles [20] over very short time scales, however due to the long wavelength of the probe, atomic scale motions cannot be measured without relying on interpretations from continuum elasticity theory. Pump-probe experiments on nanoparticles using electrons or X-rays overcomes this problem by probing the atomic scale motions directly [3,21]. The low scattering cross-sections of X-rays and (relatively) low number of photons in the ultra-short X-ray pulses from plasma sources (required for the short pulse duration) limits the ability to study individual nanoparticles. Likewise for electrons, the number of electrons per ultrashort pulse has meant probing individual nanoparticles has been difficult. The increased flux of synchrotron sources in comparison to plasma sources provides sufficient X-ray photons to probe individual nanoparticles but at the expense of time resolution. Probing of individual particles also allows in-depth studies of the mechanical response of particles with defects or very specific structure. This is particularly important for investigations of surface melting where the presence of occlusions or defects could act as nucleation points for the melting with the possible formation of core-shell structures[22]. Additionally, the role of defects and surface morphology on bond-softening in individual particles [22] could be investigated. These applications, among many others, provide strong motivation for us to develop ultrafast pump-probe X-ray diffraction methods

on individual nanocrystals using X-ray free electron lasers (XFELs). The data obtained, using this approach can elucidate the elastic response of the atomic lattice to laser irradiation while simultaneously obtaining high-resolution real-space images of the deformation field inside the nanocrystal using Bragg coherent diffraction imaging (BCDI) [23].

BCDI is sensitive to very small variations in strain within nano-crystals since it recovers the projected distortion of the electron density with pico-meter (pm) sensitivity. The recovered image comprises the amplitude, which is related to the electron density, and the phase, $\phi(\boldsymbol{r})$, which is related to the (vector) displacement field $\boldsymbol{u}(\boldsymbol{r})$ of the atoms from the ideal lattice points and the scattering vector, $\boldsymbol{Q}$ via $\phi(\boldsymbol{r}) = \boldsymbol{u}(\boldsymbol{r}) \cdot \boldsymbol{Q}$ (see Supplementary Information). Images obtained from non-coplanar Bragg peaks can be combined to recover the full displacement field [24].

Figure 1 shows a schematic of the experimental arrangement for ultrafast BCDI, which was performed at the X-ray pump probe (XPP) end station at the Linac Coherent Light Source (LCLS). Gold nanocrystals, approximately 300-400 nm in diameter (see Methods Summary) were placed at the center of a diffractometer. A Ti-Sapphire laser of wavelength 800 nm and pulse length of 50 fs (full-duration at half-maximum, FDHM) was used to generate coherent acoustic phonons in the gold nanocrystals. The incident fluence used in the experiment was 1 $\mu$J/cm$^2$. The sample was illuminated with monochromatic 1.347 Å (9.2 keV) X-rays generated by the LCLS operating at a repetition rate of 120 Hz with each pulse being approximately 80 fs long (FDHM). Beryllium lenses were used to focus the illumination onto the sample to an approximately $30 \times 30 \ \mu$m$^2$

spot. Multiple nanocrystals are illuminated simultaneously, but orientation differences between them allows Bragg peaks from individual nanocrystals to be spatially separated on the detector. The relative timing (accurate to sub ps) of the optical and X-ray pulse was adjusted to provide the time-resolved data with the two beams almost parallel for spatial coincidence. Both fluences were below the damage threshold to allow repeated measurements. The coherent diffraction patterns were recorded using a Cornell-SLAC pixel array detector (CS-PAD) positioned 1.2 m from the sample at the gold (111) Bragg peak, a sufficient distance to over-sample [8] the diffraction patterns. A helium filled bag was placed between the sample and detector to reduce air scatter.

Shown in Fig. 2a and b are examples of the coherent diffraction patterns that were recorded from individual nanocrystals. The diffraction patterns clearly show the modulated diffraction fringes due to the coherent illumination and finite sample size, which was much smaller than the X-ray beam. The fringes are most prominent in the facetted directions of the nanocrystal. The diffraction pattern collected immediately before the pump laser (Fig. 2a) shows a relatively symmetric fringe pattern, while the diffraction pattern +60ps after (Fig. 2b) shows a more asymmetric diffraction pattern which is attributed to inhomogenous lattice distortions i.e. an elastic strain gradient. Homogenous contraction and expansion of the lattice (radial breathing modes) manifests itself as a shift of the entire diffraction pattern (see Supplementary Information) as the average lattice spacing changes across the nanocrystal. Shown in Fig. 2c and d is the angular shift of the gold (111) Bragg peak for two nanocrystals, A and B. For each time delay, the center of mass from the sum of 100 diffracted LCLS pulses was used to obtain the angular shift, with the error for each delay point given by the

standard deviation. At the center of the rocking curve, $\sim 10^4$ diffracted photons are recorded per pulse. The homogenous lattice expansion and contraction is evident as harmonic motion of the Bragg peak angular shift. Immediately after the arrival of the optical pump laser (positive delay times) the diffraction pattern starts shifting to lower angles. Because the crystal is much bigger than the electromagnetic "skin depth", this behaviour is only consistent with an electron-mediated model, such as the "Two-temperature" model [25] of heating in which electrons are excited first and subsequently transfer energy to the lattice through electron-phonon coupling. Also plotted (solid red line), is the fitted peak shift, $S(\tau)$, as a function of delay time, $\tau$, and is given by

$$S\left(\tau\right) = \sum_{n=1}^{N} A_n \exp\left[-\frac{\tau}{\tau_{d,n}}\right] \cos\left[\frac{2\pi}{T_n}\left(\tau + \tau_{0,n}\right)\right] + C_n. \tag{1}$$

$n$ is the mode number, $N(=2)$ is the total number of fitted modes, $A$ is the amplitude, $\tau_d$ is the decay time, $T_n$ is the period of the oscillation and $\tau_0$ is the time offset. Two oscillation modes are sufficient to fit the data shown in Fig. 2c and d within their errors with the fitted parameters summarised in Supplementary Table 1. The fitted values of the two periods from the data for nanocrystal A were 101 ps and 241 ps and for nanocrystal B were 90 ps and 256 ps. These two oscillation modes are well reproduced by a Molecular Dynamics (MD) simulation (see Supplementary Information) shown in Supplementary Fig. 1. Using the thermal expansion coefficient for bulk gold of $14.4(2)\times10^{-6}\mathrm{K}^{-1}$ and the maximum change in the lattice constant, the temperature increase on each pump-probe cycle was estimated to be 44 K for each of the two nanocrystals. The fitted vibration amplitudes correspond to a maximum displacement of 600pm at the surface of the crystal.

The peak position versus delay time shown in Fig. 2 agrees well with previous studies of gold nanoparticles [18,22,26] or thin films [13]. However, the important distinction in this study is that we are able to monitor the behaviour of *individual* nanocrystals using X-ray diffraction rather than the behaviour of an ensemble [18,22,26]. X-rays provide the structural sensitivity evident in Fig. 2c and d where both in-plane and out-of-plane cylinder oscillations are observed owing to the fact the $Q$ vector couples to both these directions. Importantly, the relatively long lifetime of the oscillations in comparison to previous studies can be attributed to the fact that there is no ensemble average of heterogeneous periods in our experiment [18–20] (see Supplementary Information).

Thus far, we have identified two clear vibration modes in the expansion of the crystal. Further modes, such as shear modes, can only be identified by imaging the crystal distortions directly because these do not result in a shift of the Bragg peak position. Three dimensional (3D) images as a function of delay time were obtained for nanocrystal A by collecting 3D coherent diffraction patterns and then recovering the lost phase information using phase retrieval [27](see Methods Summary). The homogenous (linear) lattice expansion and contraction due to the breathing modes of the nanocrystal have been removed (see Supplementary Information) leaving only the inhomogenous component which would manifest itself as a broadening/distortion of the Bragg peak rather than a peak shift.

Figure 3 shows images of the phase of nanocrystal A, displayed as orthogonal cuts through the center for selected times. This phase is the change in the displacement of the crystal, projected

onto the diffraction vector $Q$, whose direction is also shown in Fig. 3. To emphasise the changes, we have subtracted the image at -40 ps from the subsequent times, which removes the contribution of small static residual stresses in the nanocrystal. The spatial pattern of oscillating regions of expansion and contraction are well within the resolution of the image (see Methods Summary), estimated as $51 \pm 7$ nm, $22 \pm 3$ nm and $55 \pm 6$ nm in the x, y and z directions respectively.

What is particularly evident in Fig. 3 is that the regions of expansion become regions of contraction and vice versa as the delay time increases. This spatial and temporal reversal of expansion and contraction is indicative of the presence of a shear vibration mode of higher order than a simple breathing mode. We compare this pattern of displacements with the theoretical (1,1) shear mode of a cylinder with a radius of 200 nm and a height of 220nm (see Supplementary Information for details), which is compared with the experimental images in Fig. 4 at +110ps delay time. The good agreement between the data and the theory strongly supports the presence of this otherwise invisible higher order mode. A comparison can also be made with Supplementary Fig. 2 which compares the data to a MD simulation. Our observation of this 50pm amplitude mode in the presence of a 600pm breathing mode, shows the significant sensitivity gain by BCDI imaging.

The combination of intense, coherent and ultra-short X-ray pulses provided by XFEL's has enabled direct, unambiguous imaging of coherent acoustic phonons in gold nanocrystals in three dimensions. We have been able to image a higher order phonon mode in a single gold nanocrystal over ps time scales which agrees well with a (1,1) shear mode in a cylinder and with our MD

simulations. The ability to spatially resolve inhomogenous lattice distortions over very short time scales is an invaluable tool to investigate fundamental phenomena such as coherent phonon generation and propagation, melting and phase transitions. The technique demonstrated here can be applied widely to investigate other materials such as semiconductors and nano structures. Many other applications will become possible with the advent of coherent, ultrashort electron sources [28] which could provide atomic scale images when used with diffractive imaging.

## Methods Summary

**Sample preparation.** A 2 nm layer of titanium was deposited using thermal evaporation onto an silicon wafer followed by 20 nm of gold. The thin film was then annealed in air at 1000°C for approximately 10 hours after which time the film had dewetted and formed nanocrystals.

**Experiment.** The experiment was performed at the XPP instrument at the LCLS. A 1520×1520 pixel CS-PAD with 110 $\mu$m square pixels was used to record the diffraction. The Beryllium lenses were positioned so that the sample position was out of the nominal focus. This regime was chosen so that the X-ray pulses from the LCLS did not destroy the sample. Damage from either the optical or X-ray pulses was monitored using a confocal microscope (Olympus LEXT) mounted directly above the sample. To record the 3D diffraction pattern, the nanocrystals were rocked in 41 0.02° steps. At each position, 1000 diffraction patterns were recorded. Filtering of the data was done *ex post facto* to remove saturated frames and blank shots, with the final summed patterns consisting of the 100 brightest, non-saturated shots (see Supplementary Information).

**Phase Retrieval** Phase retrieval was performed using a guided approach[29]. 15 random starts were initiated with each member being subjected to 10 iterations of error reduction [27] followed by 160 iterations of hybrid-input output [27] and then a further 30 iterations of error reduction. After this first generation, the best iterate was selected and used to generate a further 15 new iterates[29]. This process was repeated for a total of 5 generations with the final solution comprising the average of the 5 best iterates. After the phase retrieval was completed, transformation of the image to an orthogonal laboratory frame was performed with the details found elsewhere [30]. The final resolution was calculated on the transformed image by taking a line-out and fitting a Gaussian to its derivative. The resolution is given as the full-width at half maximum of this Gaussian. This was repeated for each of the orthogonal directions.

## References

1. Shank, C. V., Yen, R. & Hirlimann, C. Femtosecond-time-resolved surface structural dynamics of optically excited silicon. *Phys. Rev. Lett.* **51**, 900–902 (1983).

2. Rose-Petruck, C. *et al.* Picosecond-milliangstrom lattice dynamics measured by ultrafast x-ray diffraction. *Nature* **398**, 310–312 (1999).

3. Ruan, C.-Y., Murooka, Y., Raman, R. K. & Murdick, R. A. Dynamics of size-selected gold nanoparticles studied by ultrafast electron nanocrystallography. *Nano Letters* **7**, 1290–1296 (2007).

4. Siders, C. W. Detection of Nonthermal Melting by Ultrafast X-ray Diffraction. *Science* **286**,

1340–1342 (1999).

5. Siwick, B. J., Dwyer, J. R., Jordan, R. E. & Miller, R. J. D. An atomic-level view of melting using femtosecond electron diffraction. *Science (New York, N.Y.)* **302**, 1382–5 (2003).

6. Fritz, D. M. *et al.* Ultrafast bond softening in bismuth: Mapping a solid's interatomic potential with x-rays. *Science* **315**, 633–636 (2007).

7. EmmaP. *et al.* First lasing and operation of an angstrom-wavelength free-electron laser. *Nat Photon* **4**, 641–647 (2010).

8. Miao, J., Charalambous, P., Kirz, J. & Sayre, D. Extending the methodology of x-ray crystallography to allow imaging of micrometre-sized non-crystalline specimens. *Nature* **400**, 342 (1999).

9. Loh, N. D. *et al.* Fractal morphology, imaging and mass spectrometry of single aerosol particles in flight. *Nature* **486**, 513–517 (2012).

10. Seibert, M. M. *et al.* Single mimivirus particles intercepted and imaged with an x-ray laser. *Nature* **470**, 78–81 (2011).

11. Lindenberg, A. *et al.* Time-resolved X-Ray diffraction from coherent phonons during a laser-induced phase transition. *Physical review letters* **84**, 111–4 (2000).

12. Sokolowski-Tinten, K. *et al.* Femtosecond X-ray measurement of coherent lattice vibrations near the Lindemann stability limit. *Nature* **422**, 287–9 (2003).

13. Chen, J., Chen, W.-K., Tang, J. & Rentzepis, P. M. Time-resolved structural dynamics of thin metal films heated with femtosecond optical pulses. *Proceedings of the National Academy of Sciences of the United States of America* **108**, 18887–92 (2011).

14. Cavalleri, a. *et al.* Tracking the motion of charges in a terahertz light field by femtosecond X-ray diffraction. *Nature* **442**, 664–6 (2006).

15. Turner, M. *et al.* Selective oxidation with dioxygen by gold nanoparticle catalysts derived from 55-atom clusters. *Nature* **454**, 981–983 (2008).

16. Maier, S. A. *et al.* Plasmonics—a route to nanoscale optical devices. *Advanced Materials* **13**, 1501–1505 (2001).

17. S., H. *et al.* Single-protein nanomechanical mass spectrometry in real time. *Nat Nano* **7**, 602–608 (2012).

18. Hartland, G. V. Coherent vibrational motion in metal particles: Determination of the vibrational amplitude and excitation mechanism. *The Journal of Chemical Physics* **116**, 8048–8055 (2002).

19. Pelton, M. *et al.* Damping of acoustic vibrations in gold nanoparticles. *Nat Nano* **4**, 492–495 (2009).

20. van Dijk, M. A., Lippitz, M. & Orrit, M. Detection of acoustic oscillations of single gold nanospheres by time-resolved interferometry. *Phys. Rev. Lett.* **95**, 267406 (2005).

21. Plech, a., Kotaidis, V., Grésillon, S., Dahmen, C. & von Plessen, G. Laser-induced heating and melting of gold nanoparticles studied by time-resolved x-ray scattering. *Physical Review B* **70**, 1–7 (2004).

22. Hartland, G. V., Hu, M., Dame, N. & Sader, J. E. Softening of the Symmetric Breathing Mode in Gold Particles by Laser-Induced Heating 7472–7478 (2003).

23. Pfeifer, M. A., Williams, G. J., Vartanyants, I. A., Harder, R. & Robinson, I. K. Three-dimensional mapping of a deformation field inside a nanocrystal. *Nature* **442**, 63–66 (2006).

24. Newton, M. C., Leake, S. J., Harder, R. & Robinson, I. K. Three-dimensional imaging of strain in a single zno nanorod. *Nat Mater* **9**, 279–279 (2010).

25. Allen, P. B. Theory of thermal relaxation of electrons in metals. *Phys. Rev. Lett.* **59**, 1460–1463 (1987).

26. Ichiyanagi, K. *et al.* Laser-induced picosecond lattice oscillations in submicron gold crystals. *Physical Review B* **84**, 1–5 (2011).

27. Fienup, J. R. Phase retrieval algorithms - a comparison. *Appl. Opt.* **21**, 2758–2769 (1982).

28. McCulloch, A. J. *et al.* Arbitrarily shaped high-coherence electron bunches from cold atoms. *Nat Phys* **7**, 785–788 (2011).

29. Chen, C.-C., Miao, J., Wang, C. W. & Lee, T. K. Application of optimization technique to noncrystalline x-ray diffraction microscopy: Guided hybrid input-output method. *Phys. Rev. B* **76**, 064113 (2007).

30. Clark, J. N., Huang, X., Harder, R. & Robinson, I. K. High-resolution three-dimensional partially coherent diffraction imaging. *Nat Commun* **3** (2012).

**Author contributions**    The LCLS experiment was carried out by J. N. C., L. B., D. M. F., H. T. L., D. Z., M. C., G. J. W., S. B., M. M., B. A., R. J. H., A. M. K., J. S. W. and I. K. R.. Data analysis was performed by J. N. C. and I. K. R.. MD simulations were performed by A. H. and J. S. W.. The manuscript was prepared by J. N. C. and I. K. R. with contributions from all authors. Samples were prepared by G. X., J. N. C. and L. B.. The confocal alignment system was conceived by I. K. R. and R. J. H..

**Additional information**    The authors declare no competing financial interests. Correspondence and requests for materials should be addressed to J.N.C. (email: jesse.clark@ucl.ac.uk) or I.K.R (email: i.robinson@ucl.ac.uk).
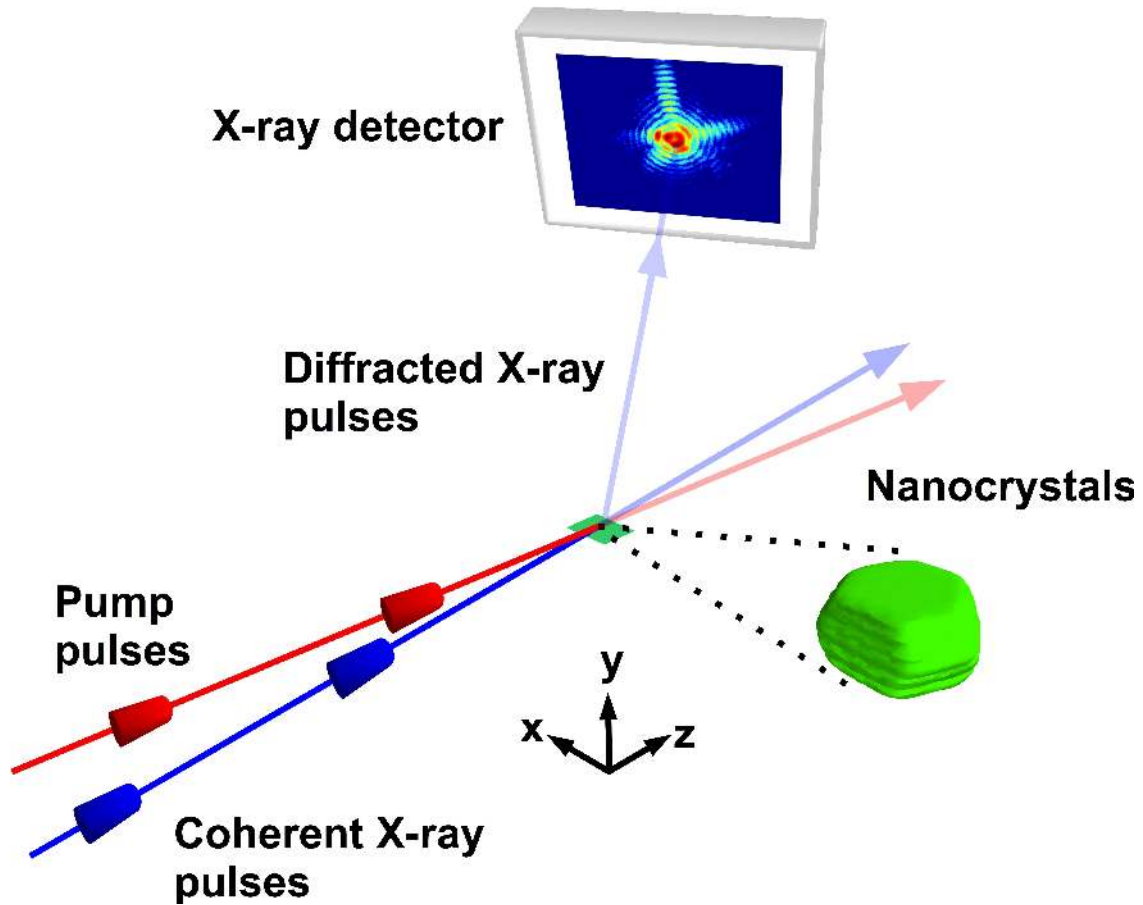
Figure 1: **Schematic of the setup for ultrafast time resolved Bragg coherent diffraction imaging.** Optical pulses (red) perturb the sample, generating phonons. Coherent X-ray pulses (generated from an XFEL) arrive a short time later where the diffracted pulses are recorded using a CS-PAD area detector.
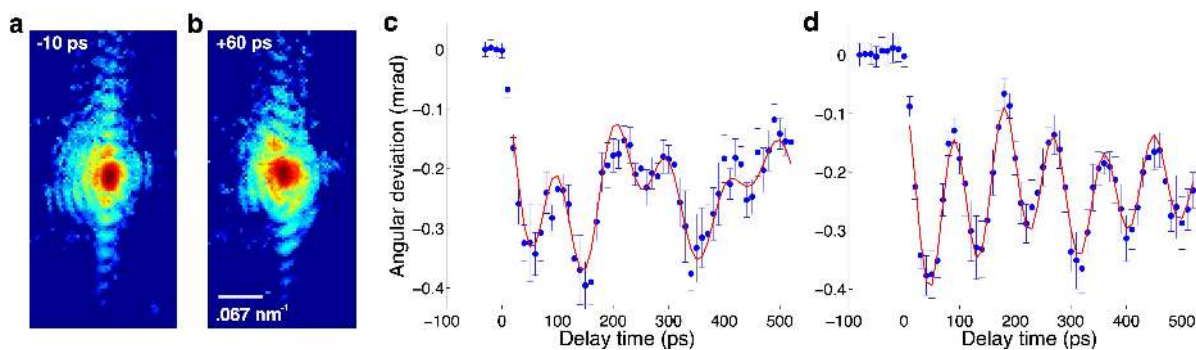
Figure 2: **Time resolved Bragg coherent diffraction data from single nanocrystals.** a,b, Experimentally recorded coherent diffraction patterns from a single nanocrystal for delay times of -10 ps and +60 ps respectively. The diffraction patterns are the sum of 100 shots and are scaled logarithmically. c, Gold (111) Bragg peak angular shift as a function of delay time from the same nanocrystal. d) Angular shift as a function of delay time from a different nanocrystal. The blue dots are the experimental data and the solid red line is the modelled peak shift.
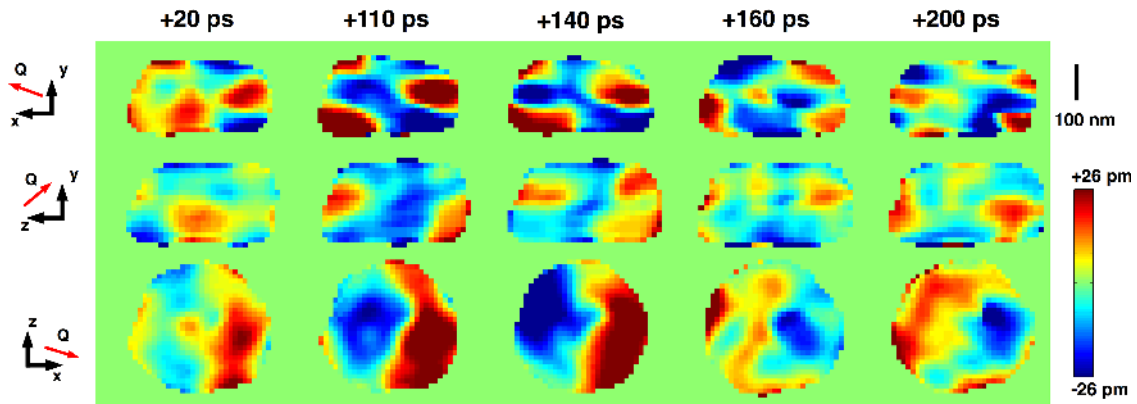
Figure 3: **Imaging of acoustic phonons in a nanocrystal.** Orthogonal cut planes through the nanocrystal showing the projected displacement as a function of delay time. For each delay time orthogonal slices taken from the center of the nanocrystal are shown. The direction of the displacement field is given by the $Q$ vector in red. It should be noted that the range of displacement has been truncated to $\pm26$pm instead of the full range of $\pm53$pm for clarity.
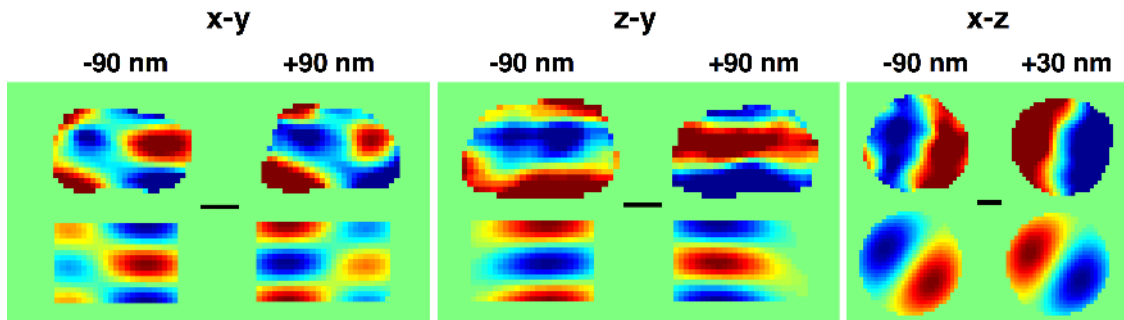


Figure 4: **Comparison of data with simulation** Orthogonal cut planes comparing the +110 ps delay time (top) with a simulated (1,1) mode for a cylinder (bottom). Two slices for each viewing direction are shown, taken either side of the center of nanocrystal A. The black bar indicates a scale of 100 nm.